

Sorting photon wave packets using temporal-mode interferometry based on multiple-stage quantum frequency conversion

D. V. Reddy,¹ M. G. Raymer,^{1,*} and C. J. McKinstrie²

¹*Oregon Center for Optics, Department of Physics,
University of Oregon, Eugene, Oregon 97403, USA*

²*Applied Communication Sciences, Red Bank, New Jersey 07701, USA*
(Dated: February 26, 2022)

All classical and quantum technologies that encode in and retrieve information from optical fields rely on the ability to selectively manipulate orthogonal field modes of light. Such manipulation can be achieved with high selectivity for polarization modes and transverse-spatial modes. For the time-frequency degree of freedom, this could efficiently be achieved for a limited choice of approximately orthogonal modes, i.e. non-overlapping bins in time or frequency. We recently proposed a method that surmounts the selectivity barrier for sorting arbitrary orthogonal temporal modes [Opt. Lett. **39**, 2924 (2014)] using cascaded interferometric quantum frequency conversion in nonlinear optical media. We call this method temporal-mode interferometry, as it has a close resemblance to the well-known separated-fields atomic interferometry method introduced by Ramsey. The method has important implications for quantum memories, quantum dense coding, quantum teleportation, and quantum key distribution. Here we explore the inner workings of the method in detail, and extend it to multiple stages with a concurrent asymptotic convergence of temporal-mode selectivity to unity. We also complete our analysis of pump-chirp compensation to counter pump-induced nonlinear phase-modulation in four-wave mixing implementations.

I. INTRODUCTION

The state of a photon is fully characterized by its helicity, and the three components of its momentum. For guided photons or photons in beam-like geometries, the same degrees of freedom may be stated as polarization, transverse-mode profile, and energy (or frequency) [1]. Polarization spans a two-dimensional state space, allowing definitions of two-tuple orthogonal basis sets, for example perpendicular linear polarization states. Sorting and the application of unitary transformations on any choice of bases is accomplished through combinations of existing tools such as polarizing beam splitters, half-wave plates, and quarter-wave plates. Transverse modes are two-dimensional functions, and may be expressed in the basis of orbital angular momentum, transverse-spatial parity, or integer indices denoting eigenfunctions of some guiding geometry. In contrast to polarization, transverse modes offer a multidimensional state space, and their selective manipulation has been an active subject of recent studies [2–9].

For traveling (longitudinally unconstrained) fields, energy (or frequency) is a continuous-variable degree of freedom. This spans an infinite dimensional space, and high-fidelity selective sorting (and by extension, any unitary operation) on arbitrary states in this space has traditionally been limited to specific choices of basis sets. If the considered states have disjoint spectra, this is accomplished using a prism or diffraction grating. That is the basis of wavelength-division multiplexing in optical communication systems. Sorting has also been accomplished for spread-spectrum distributions of orthogonal

frequency subcarriers via orthogonal-frequency-division-multiplexing (OFDM) [10], and for partially overlapping temporal pulses of a specific shape and temporal offset via orthogonal-time-division-multiplexing (OTDM) [11]. But orthogonal states can also be defined as superpositions over a continuum of frequencies with overlapping spectra. By Fourier transformation, such states can be represented in the time domain, thereby introducing the idea of ‘temporal modes’—a set of orthogonal functions of time that form a complete basis for representing an arbitrary state in the energy degree of freedom [1, 12].

Temporal modes (TMs) are a prime contender for the preferred basis for mapping qubits or higher-dimensional qudits onto photons, because their orthogonality is immune to chromatic dispersion and polarization rotation. TMs are ideal for transmission in waveguides and optical fibers with no cross-talk: since all TMs at a given central frequency suffer the same unitary evolution under linear dispersion, their orthogonality is maintained in long-distance quantum communication through time-stationary guided media.

The most promising approach to the sorting of light into a discrete set of TMs has been nonlinear wave mixing with pulsed pumps [13, 14]. From a general mathematical standpoint analogous to that in [15], it is clear that temporal wave-packet multiplexing is possible only by using a temporally nonstationary process that acts on field amplitudes, not intensities. This is inherently true in strong-pump driven nonlinear wave mixing, where the weak signal fields need to be synchronous with a device clock, defined by the arrival time of the pump pulse. Nonzero relative group velocities between participating fields also allow the device to “sample” or “measure” the complex temporal amplitude of the signals via a continuously shifting inter-pulse temporal overlap, which is essential if it

* raymer@uoregon.edu

needs to discriminate between orthogonal modes. The complex envelopes of the strong pump pulses provide for a means of programming the device to sort user-defined temporal modes. Such a system can be called a complex-pulse-envelope gate, or pulse gate for short [14]. It has also been called a field-orthogonal TM sorter [16].

It was first pointed out in [13] that quantum frequency conversion (QFC) by four-wave mixing (FWM) is partially TM-selective when using short pump pulses. The same is true also for QFC by three-wave mixing (TWM) driven by a single pump pulse, as pointed out by Eckstein et al, and proposed as a general method of TM sorting and multiplexing for quantum information applications [14]. The idea is to design the process so that only a single temporal mode among the orthogonal set has its frequency converted; then a simple frequency-selective component (diffraction grating, prism, etc.) could easily separate the converted wave packet from the unconverted ones. Recent studies furthered the concept of using optical frequency conversion (FC) by nonlinear wave mixing for creating TM-mode-selective devices [17–20]. The role of FC in quantum optical communication networks has been reviewed in [21].

Ideally, the device should frequency convert a user-specified temporal mode component from the input field into the output mode in a different frequency band without ‘contamination’ by other temporal mode components of the input field in the orthogonal subspace. But it was found through careful modeling that the basic single-stage QFC process is fundamentally limited to a TM ‘selectivity’ of no greater than about 0.8, strongly limiting its usefulness [14, 17, 19, 20, 22]. High selectivity is a necessary condition for scalability in quantum applications, and a value of 0.8 falls short of error-tolerance estimates in both quantum communication and computing. The limit exists as a fundamental feature of group-velocity mismatched inter-pulse dynamics in a dispersive medium, as will be shown. We discovered that a generalization of the QFC schemes (either FWM or TWM) can circumvent this limit and achieve essentially perfect TM sorting, with a selectivity approaching unity [16]. The new scheme uses two or more spatially separated stages of QFC, with the effects of the stages adding coherently. We named this scheme *temporal-mode interferometry* (TMI), as it has a close resemblance to the separated-fields atomic interferometry method introduced by Ramsey [23]. In that case, an atom passes through two separated laser beams. The first field partially excites the atom (for example, to 50% probability), and the second field, depending on its phase relative to that of the oscillating atomic dipole resulting from the first field, either further excites the atom (for example, to 100%) or fully deexcites the atom back to its ground state. The present case of TMI is more complex, in that the traveling pulse is not localized at a point like a typical atom, but undergoes temporal shaping as its frequency is being converted. Time-domain versions of Ramsey interference are also known in the contexts of photon-echo experiments and atomic-fountain clocks

[24, 25].

The dependence of conversion efficiency on the relative phases of the signal and control fields is what earns the TMI method the name interferometry. It is useful for real-time control and switching of various temporal modes. The concept of two-stage QFC, and its analogy to Ramsey interferometry, was subsequently independently developed by Clemmen et al [26], but only in the context of continuous-wave fields, so in this case it lacks the TM selectivity that is the main thrust of the present discussion.

This paper details and expands the work reported in [16]. In particular, we present the theory of inter-stage mode matching. We explore the dependence of mode selectivity on the ratio of interaction-time and pump temporal duration in TWM. We provide the theory of pump-chirp compensation in FWM, including a family of analytical expressions for pump chirps. Finally, we give numerical demonstrations of multistage (more than two) TMI and the associated asymptotic gains in mode selectivity.

II. II. TEMPORAL MODES

Temporal modes are a set of complex functions that are orthogonal in time (or frequency), which form a complete basis for representing an arbitrary state in the energy degree of freedom [1, 12]. The state can be expressed as a coherent superposition of many possible frequency states,

$$|\psi_j\rangle = \frac{1}{2\pi} \int d\omega \tilde{\psi}_j(\omega) \hat{a}^\dagger(\omega) |vac\rangle = \hat{b}_j^\dagger |vac\rangle, \quad (1)$$

$$[\hat{a}(\omega), \hat{a}^\dagger(\omega')] = 2\pi\delta(\omega - \omega'), \quad [\hat{b}_j, \hat{b}_k^\dagger] = \delta_{j,k},$$

where $\hat{a}^\dagger(\omega)$ creates a monochromatic photon with frequency ω . By Fourier transform, the same state can be expressed as a coherent quantum superposition state of many possible ‘creation times,’ that is

$$|\psi_j\rangle = \int dt \psi_j(t) \hat{A}^\dagger(t) |vac\rangle, \quad (2)$$

where $\hat{A}^\dagger(t)$ creates a broadband photon at time t . The TM mode functions $\psi_j(t)$ fully overlap in time, but are orthogonal with respect to a time integral. Likewise in the frequency domain. The mode basis sets $\{\psi_j(t)\}$ (or $\{\tilde{\psi}_j(\omega)\}$) can be any user-defined orthonormal set. The integer index is in principle unbound, reflecting the infinite dimensionality of a continuous variable degree of freedom. For exceptionally broadband TMs, covering essentially the entire visible spectrum, exact orthogonality is not ensured [1]. But this subtlety will have negligible effects on practical systems where channels are defined with bandwidths that are narrow compared to the carrier frequencies.

TM-based multiplexing has more in common with code-division multiplexing, as the different overlapping functions serve as spread-spectrum codes that mark information channels. This is in contrast with conventional time- or frequency-based optical multiplexing, which use either separated short pulses or narrow spectral windows to define different information channels (fig. 1).

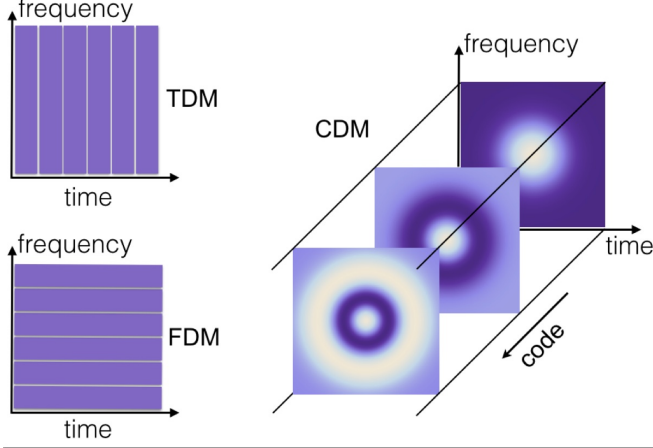


FIG. 1. Time- and frequency-division multiplexing being contrasted with code-division multiplexing (CDM), with different codes represented by time-frequency Wigner functions for orthogonal temporal modes. The choice of the temporal-mode set is not unique.

III. SINGLE-STAGE QUANTUM FREQUENCY CONVERSION

Here, we present the theory for QFC via three-wave mixing (TWM) [27–31] and four-wave mixing (FWM) [13, 32]. To model the process, we designate the participating frequency channels by s and r for the signal photons, and p (and q) for the strong pump field(s). We denote square-normalized classical field envelopes in the j channel by $A_j(z, t)$. Quantum mechanically, $A_j(z, t)$ represent the field annihilation operators for a wave-packet mode of that central frequency (ω_j) and envelope shape [1] and obey the same equations of motion as their classical counterparts [13, 19]. Then the equations of motion for QFC are [33, 34]:

$$(\partial_z + \beta'_p \partial_t) A_p = i(\gamma/2) \delta_F [|A_p|^2 + 2 |A_q|^2] A_p, \quad (3a)$$

$$(\partial_z + \beta'_q \partial_t) A_q = i(\gamma/2) \delta_F [2 |A_p|^2 + |A_q|^2] A_q, \quad (3b)$$

$$(\partial_z + \beta'_r \partial_t) A_r = i\gamma A_p A_q^* A_s + i\gamma \delta_F [|A_p|^2 + |A_q|^2] A_r, \quad (3c)$$

$$(\partial_z + \beta'_s \partial_t) A_s = i\gamma A_p^* A_q A_r + i\gamma \delta_F [|A_p|^2 + |A_q|^2] A_s, \quad (3d)$$

where $\beta'_j \equiv [d\beta/d\omega]|_{\omega=\omega_j}$ are the group slownesses (inverse group velocities), and we have neglected higher-order dispersion, which is valid for sufficiently narrow-band pulses. The self- and cross-phase modulation factor δ_F is 0 for TWM and 1 for FWM. γ is the product of the effective $\chi^{(2)}$ or $\chi^{(3)}$ nonlinearity and the square roots of the pump-pulse energies. For TWM, $A_q(z, t) \equiv 1$. The presence or absence of complex-conjugation of pump amplitudes follows the convention that $\omega_r = \omega_p + \omega_s - \omega_q$ for FWM, and $\omega_r = \omega_p + \omega_s$ for TWM. The solution for Eq. (3) can be written in terms of Green functions $G_{ij}(t, t')$. For $j \in \{r, s\}$ and medium length l :

$$A_j(l, t) = \int_{-\infty}^{\infty} dt' \sum_{k=r,s} G_{jk}(t, t') A_k(0, t'). \quad (4)$$

The four kernels [17] $G_{ij}(t, t')$ comprise a generalized beam-splitter transformation, representing frequency conversion or non-conversion of each of the two possible input fields of distinct carrier frequencies [35]. The functional forms of the Green function kernels are dependent on the shapes of the p (and q) pump pulse(s). To determine the natural temporal modes for the problem, we numerically perform a singular-value decomposition (SVD), also called a Schmidt decomposition, for each $G_{ij}(t, t')$. This yields a set of singular-value functions (temporal Schmidt modes) with associated singular values (Schmidt coefficients), which we denote by ρ_n and τ_n , which satisfy $|\rho_n|^2 + |\tau_n|^2 = 1$. $|\rho_n|^2$ is the frequency conversion efficiency (CE) of the n th mode, and can be interpreted as the probability of QFC in the case of single photons. The modes are numbered in decreasing order of the Schmidt coefficients; the mode with the largest Schmidt coefficient (*i.e.* the first Schmidt mode, $n = 1$) is the target TM (expected to be selectively converted). We denote by $\phi_n(t)$ the s -input modes, and $\Psi_n(t)$ are r -output modes. In addition, there are r -input modes $\psi_n(t)$ and s -output modes $\Phi_n(t)$.

All the Green function (GF) kernels can be expressed in terms of these four mode sets as follows [35]:

$$G_{rr}(t, t') = \sum_{n=1}^{\infty} \tau_n \Psi_n(t) \psi_n^*(t'), \quad (5a)$$

$$G_{rs}(t, t') = \sum_{n=1}^{\infty} \rho_n \Psi_n(t) \phi_n^*(t'), \quad (5b)$$

$$G_{sr}(t, t') = - \sum_{n=1}^{\infty} \rho_n \Phi_n(t) \psi_n^*(t'), \quad (5c)$$

$$G_{ss}(t, t') = \sum_{n=1}^{\infty} \tau_n \Phi_n(t) \phi_n^*(t'). \quad (5d)$$

As mentioned earlier, the individual kernels are not unitary, but taken together, the complete GF is. The objective is to design a QFC device that can selectively

frequency convert or ‘drop’ the first Schmidt mode (target TM) with unit efficiency, whilst allowing 100% unconverted transmission of all orthogonal modes. The principal figure of merit for such a drop device is the ‘selectivity’ [19], defined as:

$$S = \frac{|\rho_1|^4}{\sum_{j=1}^{\infty} |\rho_j|^2}. \quad (6)$$

The best previous attempts at optimizing selectivity using a single-stage QFC scheme converged on frequency choices that are group-velocity matched, namely $\beta'_p = \beta'_s \neq \beta'_r (= \beta'_q)$ [17, 19, 34]. For FWM, this condition is easily accessed by situating the channel frequencies on either side of the zero-dispersion wavelength of the fiber, which automatically grants phase matching for a tunable set of frequencies [13]. In addition, for optimum selectivity results in FWM, the medium is required to be long enough for a complete inter-pump-pulse collision (no overlap to no overlap) [34]. However, both TWM and FWM schemes have encountered limits that are universal to generic systems governed by coupled-mode equations such as Eq. (3), and have yielded selectivities limited to around 0.8, an example of which is shown in Fig. 2. The single-stage selectivity limit arises from in the interaction between pulses convecting through each other at different speeds. The nonlinear wave-mixing is perfectly phase matched only at the central channel frequencies, and the phase mismatch acquires opposite relative signs for spectral components of the pulses below and above the central frequencies. This causes the QFC contributions of the two halves of the spectrum to beat relative to each other, which manifest as non-separable time-domain oscillations in the GF kernels [19] similar to Burnham-Chiao ringing, which occurs when a weak, resonant optical pulse propagates through an atomic vapor [36]. At high conversion, the Schmidt-mode profiles become temporally skewed relative to the group-velocity-matched pump shapes. These distortions are minimal at lower CE, enabling our two-stage scheme.

IV. IV. TEMPORAL-MODE INTERFEROMETRY

Our scheme, which we call temporal-mode interferometry, uses cascaded stages of QFC, as illustrated in Fig. 3. The method provides close to 100% TM selectivity, opening the door for manipulation of TM qubits or multi-level qudits, and may also be used for TM channel multiplexing in classical optical telecommunications. In the figure we color code the participating frequency channels s in green, and r in blue for the signal photons, as well as p (and q) the strong pump field(s) in orange (and red). Our method exploits the fact that using single-stage QFC, it is possible to discriminate orthogonal TMs nearly perfectly up to a conversion efficiency

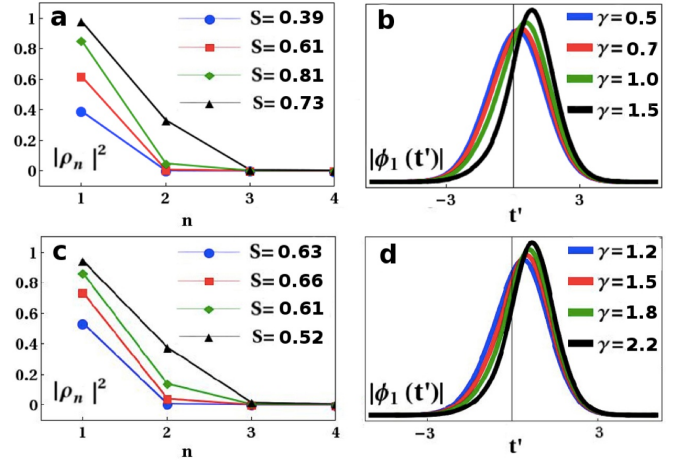


FIG. 2. Single-stage TWM (a,b) and FWM (c,d) dominant Schmidt-mode conversion efficiencies $|\rho_n|^2$ (a,c) for various pump powers, with selectivities S listed in the legend. (b,d) s -channel input Schmidt modes, illustrating increased temporal skewness with increasing γ . The values of t' are relative to a $|\beta'_r - \beta'_s|l$ of (b) 20 and (d) 10, where l is the medium length. Pump- p is Gaussian in shape.

(CE) of about 50% [17, 19]. This motivates a two-stage interferometric scheme, in which each stage is configured for 50% CE for the target TM, and functions as a 50/50 beam splitter with the r - and s -frequency channels representing its two input and output arms. An s -input photon in the target TM will be 50% frequency converted in the first stage into the r channel with a phase picked up from the pump field(s). If all fields are allowed to participate in QFC in the second stage with the right relative phases, the two effective beam splitters will function as a frequency-shifting Mach-Zehnder (or Ramsey) interferometer, allowing for complete forward or backward conversion of the state of the photon, depending on the value of the additional relative phase θ introduced between the stages. Between the two stages, the target TM component of the signal photon is in a multicolor superposition of the signal-idler frequency bands (*i.e.* a color qubit) [37, 38]. This interferometric scheme was first published by us in a previous work [16]. Phase coherence between frequency-converted and unconverted components of light has since been experimentally demonstrated for weak-coherent states by Clemmen et al [26], who independently arrived at the frequency-conversion interferometry idea. However, their implementation used continuous pumps and so is not TM selective. In our case, the interferometric frequency-conversion effect operates only on the target TM, as the orthogonal modes have negligible CE in both stages.

There are two configurations of interest: 1) ‘reversed collision’ (RC), in which the dispersion in the second-stage is inverted relative to that in the first stage, such that the relative group velocities of the pulses are reversed, and 2) ‘double collision’ (DC), in which the dis-

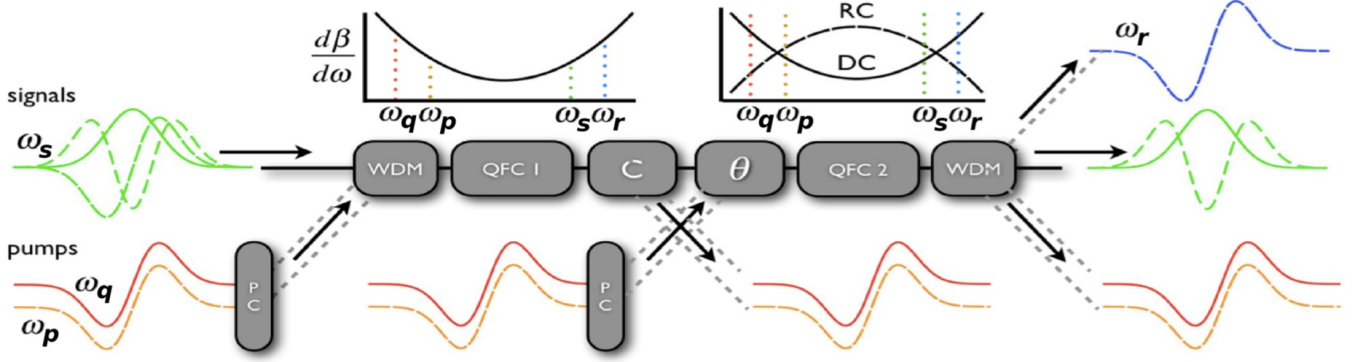


FIG. 3. Temporal-mode interferometer using two nonlinear media (QFC 1 and QFC 2) with identical (DC) or opposite-sign (RC) dispersion. Appropriate choices for pump-pulse shapes, pump powers and the phase shift θ will selectively frequency convert a specific s (green, ω_s) TM into an r (blue, ω_r) TM at a different central frequency, while not affecting temporally-orthogonal s -input TMs. The pump q is used only for $\chi^{(3)}$ implementations. WDM stands for wavelength-division multiplexer. PC stands for pre-chirp modules, which are necessary for $\chi^{(3)}$ implementations. The coupler C contains frequency dependent delays for the DC case. Reproduced from [16], with permission.

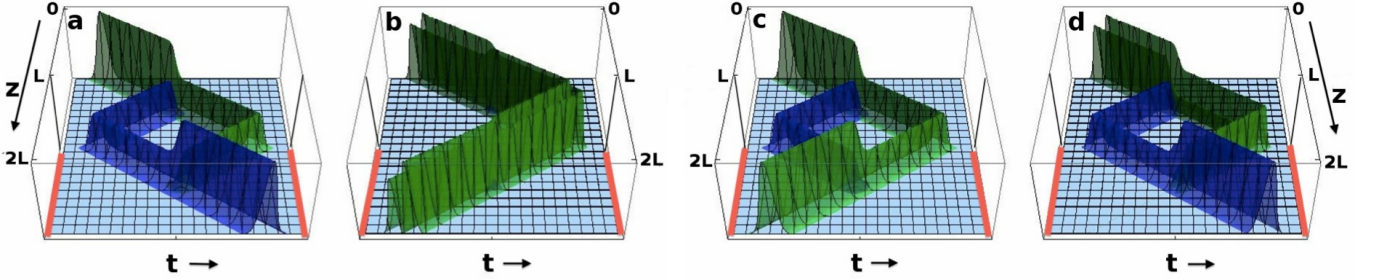


FIG. 4. Temporal-mode interferometry with the two interferometer ‘arms’ being the frequency channels s (green, lighter shade) and r (blue, darker shade), undergoing two complete collisions in the two fibers and exchanging energy. This visualization plots the color-coded signal-field intensities in the average velocity frame with populated green input and empty blue input at $z = 0$, for the RC configuration found by numerical solution of the equations of motion. (a) Both pumps are Gaussian, and the first Schmidt-mode green-to-blue conversion is nearly 100% at phase-shift $\theta = 0$. (b) Both pumps are Gaussian, and the second Schmidt-mode conversion is nearly 0%. (c) Both pumps are Gaussian, and the first Schmidt-mode conversion efficiency is suppressed to zero at phase-shift $\theta = \pi$. (d) Pump q is Gaussian, and the shape of pump p is tailored to convert the green input mode from (b) into a Gaussian-like blue output with nearly 100% efficiency at $\theta = 0$.

persion in the second-stage is identical to that in the first. In the DC case, the fast pulses must be time delayed relative to the slow pulses in between the stages so that they walk through each other again in the second stage. The inset in Fig. 3 shows the inverse group velocity vs. frequency for the two configurations. Figure 4 shows an example of TMI for the RC configuration. The necessary time delays for the DC case are implemented in the ‘coupler’ labeled C in the figure. After the target TM is frequency converted, it would be separated from the main beam using a standard wavelength-division multiplexer (WDM). As shown below, for TWM we predict in the RC case a TM selectivity of 0.9846, and in the DC case the selectivity is 0.9805, far higher than can be achieved with single-stage systems. High TM selectivity can also be achieved using FWM, but will require chirp pre-compensation of the pump pulses to be implemented in modules labeled PC, as described below.

A. Two-stage theory

For the two-stage temporal-mode interferometry, the combined Green function kernel $G_{rs}(t, t')$ is given by the interferometric equation [19]:

$$G_{rs}(t, t') = \int_{-\infty}^{\infty} dt'' [G_{rs}^{(2)}(t, t'') G_{ss}^{(1)}(t'', t') + e^{i\theta} G_{rr}^{(2)}(t, t'') G_{rs}^{(1)}(t'', t')], \quad (7)$$

where the superscripts indicate the FC process in stages 1 and 2. Functions and parameters lacking a superscript stage number characterize the combined two-stage process as a whole. For each stage separately, the ‘transmission’ (no frequency change) coefficient $\tau_n^{(\xi)}$ and the ‘reflection’ (frequency change) coefficient $\rho_n^{(\xi)}$, both taken to be real without loss of generality, independently obey relations analogous to beam-splitter rela-

tions, $\tau_n^{(\xi)2} + \rho_n^{(\xi)2} = 1$. The stage-labeled input modes are represented by lower-case functions ($\psi^{(\xi)}, \phi^{(\xi)}$) and output modes by upper case ($\Psi^{(\xi)}, \Phi^{(\xi)}$).

For TWM and FWM (with complete pump collisions), described by Eq. (3), the Schmidt coefficients are independent of pump-pulse shapes, and are determined by the value of γ . In contrast, the Schmidt mode shapes are determined by the pump-pulse shapes and the value of γ [17]. For FWM, this allows one to change the output signal shape to that of any temporal mode, if desired. For TWM, which uses of a single pump, one can influence only the Schmidt mode shapes of the group-velocity-matched signal channel.

The unitarity of the single-stage transformation imposes a pairing between the Schmidt modes across the r and s channels for that stage [35]. If the input fields for a given stage are represented as

$$A_r^{(\xi)}(t')|_{\text{in}} = \sum_n a_n \psi_n^{(\xi)}(t'), \quad (8a)$$

$$A_s^{(\xi)}(t')|_{\text{in}} = \sum_n b_n \phi_n^{(\xi)}(t'), \quad (8b)$$

then the output fields are expressed as

$$A_r^{(\xi)}(t)|_{\text{out}} = \sum_n (\tau_n^{(\xi)} a_n + \rho_n^{(\xi)} b_n) \Psi_n^{(\xi)}(t), \quad (9a)$$

$$A_s^{(\xi)}(t)|_{\text{out}} = \sum_n (\tau_n^{(\xi)} b_n - \rho_n^{(\xi)} a_n) \Phi_n^{(\xi)}(t). \quad (9b)$$

The expressions in brackets are equivalent to a beam-splitter transformation, explaining why the QFC process is considered background-free in principle [35].

The operating principle of the TMI can be summarized simply as follows. Consider the case that the input field to stage 1 is a single temporal mode $A_s^{(1)}(t)|_{\text{in}} = b_n \phi_n^{(1)}(t)$, and the r -input field is empty. Then, from Eqs. (4) and (5), the output fields of stage 1, and thus the input fields of stage 2, are

$$A_s^{(1)}(t)|_{\text{out}} = \tau_n^{(1)} b_n \Phi_n^{(1)}(t) = A_s^{(2)}(t)|_{\text{in}}, \quad (10a)$$

$$A_r^{(1)}(t)|_{\text{out}} = \rho_n^{(1)} b_n \Psi_n^{(1)}(t) = e^{-i\theta} A_r^{(2)}(t)|_{\text{in}}, \quad (10b)$$

where a phase shift θ of the r field has been introduced intentionally by the experimenter before the fields enter stage 2. Then the output of stage 2 will be

$$A_s^{(2)}(t)|_{\text{out}} = b_n \sum_{m=1}^{\infty} (\tau_m^{(2)} \tau_n^{(1)} \mu_{m,n} - e^{i\theta} \rho_m^{(2)} \rho_n^{(1)} \eta_{m,n}) \Phi_m^{(2)}(t), \quad (11a)$$

$$A_r^{(2)}(t)|_{\text{out}} = b_n \sum_{m=1}^{\infty} (\rho_m^{(2)} \tau_n^{(1)} \mu_{m,n} + e^{i\theta} \tau_m^{(2)} \rho_n^{(1)} \eta_{m,n}) \Psi_m^{(2)}(t), \quad (11b)$$

where the ‘inter-stage mode overlaps’ are defined as

$$\mu_{m,n} = \int dt \phi_m^{(2)*}(t) \Phi_n^{(1)}(t), \quad (12a)$$

$$\eta_{m,n} = \int dt \psi_m^{(2)*}(t) \Psi_n^{(1)}(t). \quad (12b)$$

If $|\mu_{n,n}| = |\eta_{n,n}| = 1$, then we say the processes in the two stages are temporally mode matched. This occurs only if the dominant output modes of stage 1 coincide with the corresponding input modes of stage 2 in each frequency channel, that is $\Phi_n^{(1)}(t) = \phi_n^{(2)}(t)$, and $\Psi_n^{(1)}(t) = \psi_n^{(2)}(t)$.

For the target mode $n = 1$, we wish to have $A_s^{(2)}(t)|_{\text{out}} = 0$ and $A_r^{(2)}(t)|_{\text{out}} = b_1 \Psi_1^{(2)}(t)$. This can only occur if several conditions are met: **1)** the non-dominant Schmidt coefficients $\rho_{n \neq 1}^{(\xi)}$ are nearly zero; **2)** the dominant processes in the two stages are temporally mode matched; and **3)** the dominant Schmidt coefficients are $\rho_1^{(\xi)} = \tau_1^{(\xi)} = \sqrt{1/2}$. Then the phase θ needs to be adjusted to zero (or some other value if the mode overlaps are complex). This gives $(\tau_1^{(2)} \tau_1^{(1)} \mu_{1,1} - e^{i\theta} \rho_1^{(2)} \rho_1^{(1)} \eta_{1,1}) = 0$ and $(\rho_1^{(2)} \tau_1^{(1)} \mu_{1,1} + e^{i\theta} \tau_1^{(2)} \rho_1^{(1)} \eta_{1,1}) = 1$. If these conditions are met, then by varying the phase of the r signal field between the fibers, either frequency channel in mode $n = 1$ can be 100% populated at the output of fiber 2.

As shown in the Numerical results section, the remaining (non-target) modes ($n \neq 1$) have $\rho_n^{(\xi)} \approx 0, \tau_n^{(\xi)} \approx 1$. So, light in any one of these modes is not significantly frequency converted in either stage, although there would be a change of temporal mode shape if $\Phi_n^{(2)}(t) \neq \phi_n^{(1)}(t)$, creating temporal mode distortion.

For many applications, especially those involving cascaded TM operations, it would be highly beneficial to implement TMI without temporal mode distortion of the non-converted signals. This is achieved if the output Schmidt modes of stage 1 match the input Schmidt modes of stage 2, that is $\Phi_n^{(1)}(t) = \phi_n^{(2)}(t)$, and $\Psi_n^{(1)}(t) = \psi_n^{(2)}(t)$ for every n . The RC configuration satisfies this requirement along with the conditions $\Phi_n^{(2)}(t) = \phi_n^{(1)}(t) = \Phi_n(t) = \phi_n(t)$ and $\Psi_n^{(2)}(t) = \psi_n^{(1)}(t) = \Psi_n(t) = \psi_n(t)$ (i.e. the output Schmidt modes are identical to the input Schmidt modes for both signal channels), leading to the elimination of temporal distortion if the non-converted input modes are identical to the input Schmidt modes of the system.

B. Numerical results

In order to derive the Green functions for QFC numerically, we implemented a coupled-mode-equation solver that accepts arbitrary input functions ($A_r(0, t')$, $A_s(0, t')$) as arguments, and computes the resultant output functions ($A_r(l, t)$, $A_s(l, t)$) for Eq. 3. This is

achieved using a fourth-order Runge-Kutta method. The solver iterates over differential steps in pulse-propagation (Δz) from $z = 0$ to l (medium length). Every iteration consists of an upwinded z -propagation scheme for all four pulses by a step (Δz), followed by a Runge-Kutta implementation of the coupled nonlinear interaction, all in spacetime domain. We compute the GF by computing the outputs for an orthogonal set of input ‘test signals’. To elaborate, consider the GF kernel and its Schmidt decomposition:

$$G_{rs}(t, t') = \sum_j \rho_j \Psi_j(t) \phi_j^*(t'). \quad (13)$$

The objective is to calculate all the individual components (ρ_j , $\Psi_j(t)$, $\phi_j(t')$) on the right-hand side. We first pick two arbitrary spanning sets of basis functions $\{B_{r,k}\}$ and $\{\tilde{B}_{s,l}\}$ and re-express the Schmidt modes:

$$\Psi_j(t) = \sum_k U_{jk} B_{r,k}(t); \quad \phi_j^*(t') = \sum_l V_{jl} \tilde{B}_{s,l}^*(t'), \quad (14)$$

$$\begin{aligned} G_{rs}(t, t') &= \sum_{k,l} \left[\sum_j U_{jk} \rho_j V_{jl} \right] B_{r,k}(t) \tilde{B}_{s,l}^*(t') \\ &= \sum_{k,l} [\bar{G}_{rs}]_{kl} B_{r,k}(t) \tilde{B}_{s,l}^*(t'). \end{aligned} \quad (15)$$

Using ($A_r(0, t) = 0$, $A_s(0, t') = \tilde{B}_{s,l}(t')$) as inputs for the solver, and decomposing the resulting r -channel outputs $A_r(l, t)$ in the $\{B_{r,k}\}$ basis, will yield the entire l th column of the complex matrix \bar{G}_{rs} . Once this matrix is determined, its Schmidt decomposition will directly reveal $\{U_{jk}\}$, $\{V_{jl}\}$, and $\{\rho_j\}$, and through them, the Schmidt modes. For all the results presented, we chose Hermite-Gaussian functions for the spanning set of basis functions for both input and output Schmidt modes, since the low-CE Schmidt modes for Gaussian pump shapes are nearly Hermite-Gaussian [18, 39].

1. Three-wave mixing

Consider the case in which the target mode is 50% converted in each stage individually while orthogonal modes remain almost completely unconverted. Then, using Eqs. (5) in Eq. (7) shows the need for inter-stage temporal mode matching between the output Schmidt modes of the first stage and the input Schmidt modes of the second stage for the scheme to work. Figure 5 shows the plots for the input and output Schmidt modes of both stages for both RC and DC configuration TMI, with a Gaussian pump, and the parameter $\zeta = |\beta'_r - \beta'_s|l/\tau_p = 200$, where l is the per stage medium length and τ_p is the Gaussian pump width. The Schmidt modes of a single channel for a given stage are found to be temporally symmetrically skewed in opposite directions between the input

and the output, the direction being dependent on the sign of $(\beta'_r - \beta'_s)$. Consequently, the inter-stage mode matching will be exact for the RC configuration, and inferior for the DC configuration. For $\zeta = 200$, the RC $\mu_{1,1}^{TWM} = \eta_{1,1}^{TWM} = 1$. But for DC, $\mu_{1,1}^{TWM} = 0.983$ and $\eta_{1,1}^{TWM} = 0.901$.

Figures 6(a-d) Schmidt modes for the RC configuration TWM-TMI for $\zeta = 200$ and a Gaussian pump. The selectivity S was computed to be 0.9846 ($|\rho_1|^2 = 0.9975$, $|\rho_2|^2 = 0.0110$). ζ is also the ratio of time-widths of the r - and s -Schmidt modes. The CE of the first four Schmidt modes (*i.e.* $|\rho_n|^2$) are plotted in green in Fig. 7(a), along with the CE of the same Schmidt modes when using a custom pump shape (magenta) tailored to ‘drop’ the second r -input Schmidt mode. Since the TWM pump can influence only the shape of the r -channel Schmidt modes, the tailored pump in Fig. 7(b) will frequency convert the second r -input Schmidt mode from Fig. 6(a) into an s -channel TM identical to the first s -output Schmidt mode from Fig. 6(d).

As an example, with a Gaussian pump, a signal photon in the r channel with shape $\psi_1(t)$ (Fig. 6(a)) will be frequency converted into an s -channel photon with shape $\Phi_1(t)$ (Fig. 6(d)), with an efficiency of $|\rho_1|^2 = 0.9975$. In contrast, a photon in the r channel with shape $\psi_2(t)$ will be frequency converted into an s -channel photon with shape $\Phi_2(t)$, with a very small efficiency of $|\rho_2|^2 = 0.0110$. In other words, an r -channel photon stays in the r channel with probability 0.9890, and will exit the device with shape $\Psi_2(t)$ (Fig. 6(b)). Figure 6(c) comes into play only if the input photon is in the s channel.

For the DC configuration with $\zeta = 200$, we computed a selectivity of 0.9805 (with $|\rho_1|^2 = 0.9957$, $|\rho_2|^2 = 0.0134$). This is slightly lower than the RC configuration due to relatively inferior inter-stage mode-matching.

Both single-stage Green function separability, and inter-stage mode matching improve asymptotically with increasing ζ , providing for corresponding gains in selectivity (Fig. 8). Larger ζ also implies a decrease in temporal skewness of the Schmidt modes relative to the pump shapes. The exact mode matching in RC configuration results in matching skewness directions for input and output Schmidt modes of a single channel, a feature that is not present for DC configuration (Fig. 9). Therefore, unconverted higher-order Schmidt modes of the RC process undergo no temporal distortion upon passing through the TMI transformation. This allows TWM-TMI devices operating in the RC configuration to be used in a chained sequence to implement multiple operations on the temporal-mode basis.

TMI is physically easier to implement in the DC configuration. A ζ of 200 can be realized, for example, in a typical 5-cm long periodically poled lithium niobate waveguide with a 70-fs pump-pulse and signal wavelengths at 795 nm and 1324 nm. RC configuration implementations rely on media with negative dispersion, which exist for $\chi^{(3)}$ -media in the form of photonic-crystal fibers, and are also possible to engineer in $\chi^{(2)}$ -media using photonic

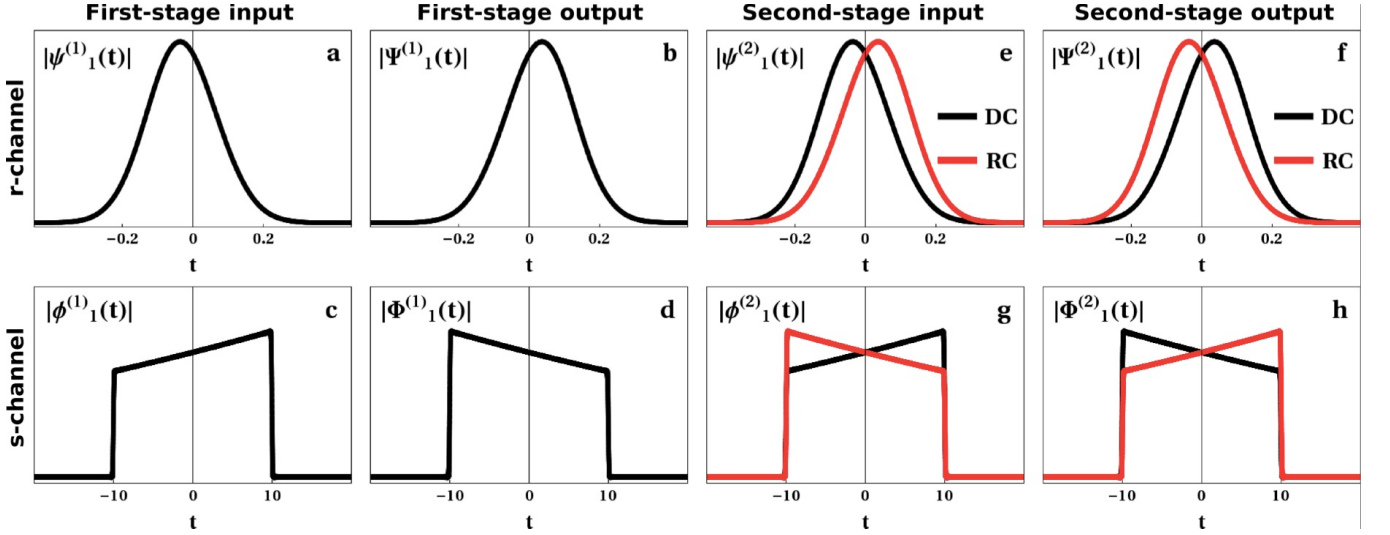


FIG. 5. The dominant input (a, c, e, g) and output (b, d, f, h) Schmidt modes for the first-(a, b, c, d) and second-(e, f, g, h) stages for both r (a, b, e, f) and s (c, d, g, h) channels for both RC (red, lighter shade) and DC (black) configurations of TWM-TMI for a Gaussian-shaped pump, and $\zeta = |\beta'_r - \beta'_s|l/\tau_p = 200$. The values of t are relative to a $|\beta'_r - \beta'_s|l$ of 20. Due to the nature of temporal skewing, the inter-stage mode-matching between the first-stage output Schmidt modes (b, d) and the second-stage input Schmidt modes (e, g) is larger for the RC than the DC configuration, thus yielding better selectivity. The complete two-stage composite system Schmidt modes for TWM-TMI in the RC configuration are plotted in Fig. 6.

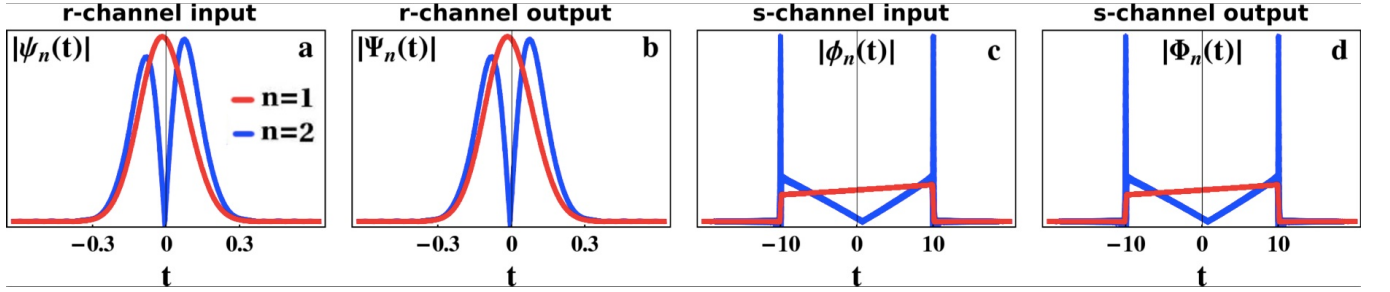


FIG. 6. Schmidt modes for TWM-TMI in the RC configuration with Gaussian pump, and $\zeta = |\beta'_r - \beta'_s|l/\tau_p = 200$, yielding a selectivity of 0.9846. The magnitudes of the first two Schmidt modes are shown for r -input (a), r -output (b), s -input (c), and s -output (d). Values of t are relative to a $|\beta'_r - \beta'_s|l$ of 20. Fig. 7 shows the conversion efficiencies of the first four Schmidt modes for two different pump shapes.

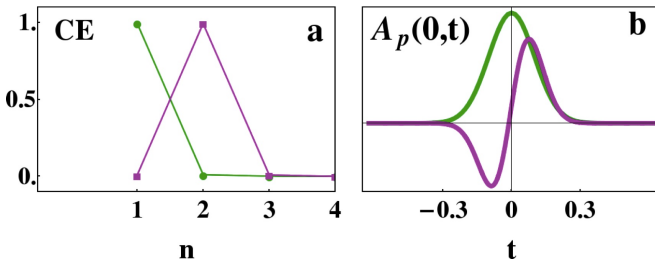


FIG. 7. (a) Conversion efficiencies for Gaussian-pumped-TWM-TMI Schmidt modes in the RC configuration. The CE for a Gaussian pump are shown in green (darker shade), and those for a custom pump shape tailored to drop the second Schmidt mode are shown in magenta (lighter shade). (b) The corresponding pump shapes shown with matching colors. Values of t are relative to a $|\beta'_r - \beta'_s|l$ of 20.

crystal waveguides [40].

TMI can also be extended to arbitrarily large number of stages in both RC and DC configurations. Since the single-stage Green functions are more separable at lower conversion efficiencies, increasing the number of stages can increase selectivity. Multistage implementations will use lower pump powers due to the increase in the number of inter-pulse interactions. For optimal selectivity when using an N -stage process, the conversion efficiency for the first stage should be approximately $0.5[1 - \cos(\pi/N)]$. The expression is the exact splitting ratio necessary for a sequence of N nonpolarizing beam splitters to interferometrically change the propagation direction of an incident beam of coherent light, and becomes more accurate for TMI for larger N . Figure 10 shows the ratio of converted-to-total energy of the first Schmidt mode versus propagation distance for various

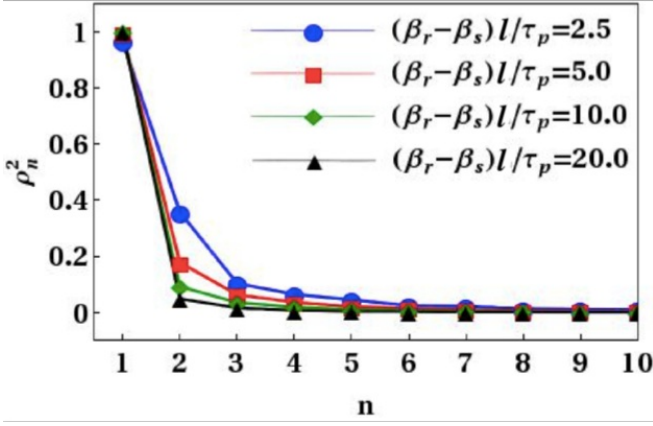


FIG. 8. Dominant Schmidt mode conversion efficiencies for TWM-TMI in the RC configuration, illustrating asymptotic improvement in selectivity with decreasing pump-pulse width τ_p relative to interaction time $(\beta'_r - \beta'_s)l$.

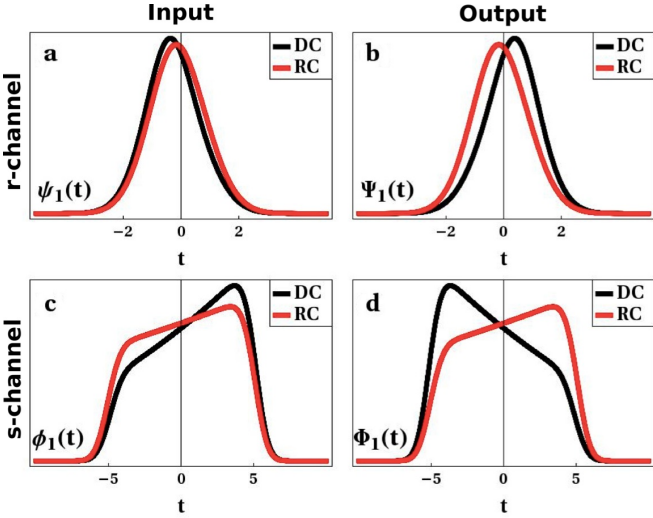


FIG. 9. The first Schmidt modes of (a) r -input, (b) r -output, (c) s -input, and (d) s -output channels for both DC (black) and RC (red, lighter shade) configurations of a two-stage TMI implemented using TWM with a single Gaussian pump, and $|\beta'_r - \beta'_s|l/\tau_p = 10$. Values of t are relative to a $|\beta'_r - \beta'_s|l$ of 10.

number of stages. The plots tend to asymptotically converge to a sinusoidal curve. A four-stage scheme yielded DC and RC selectivities of 0.9977 and 0.9978 respectively. The corresponding ten-stage selectivities are 0.99996 and 0.99997. Increasing the number of stages also decreases the temporal skewness of the first Schmidt mode relative to the corresponding pump-shape. The directionality of skewness for N -stage TWM-TMI in the DC configuration is independent of N . However, for N -stage TWM-TMI in the RC configuration, one can choose between distortionless FC and distortionless unconverted transmission of pulses by choosing odd or even N respectively.

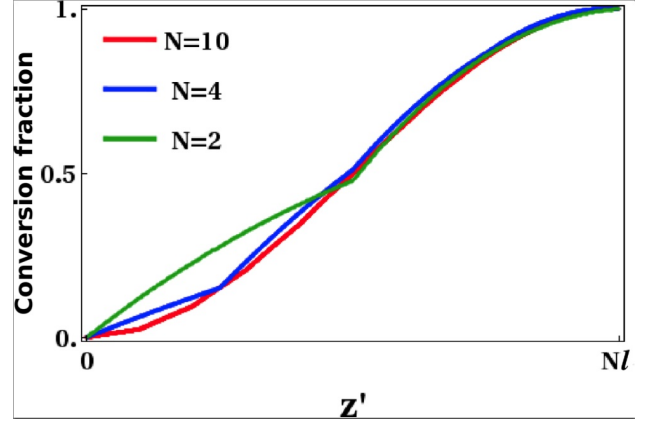


FIG. 10. Multistage TWM implementation of TMI, showing the ratio of converted to total energy of the first Schmidt mode versus z' (propagation distance). N is the number of stages and l is the medium length for each stage.

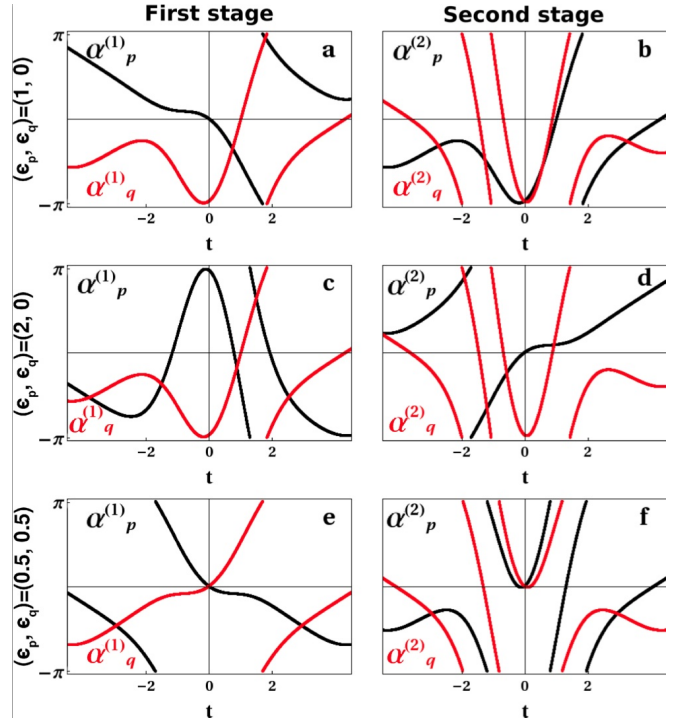


FIG. 11. The first-stage (a, c, e) and second-stage (b, d, f) pump chirps used to derive the three inter-stage mode-matched Schmid-mode phase profiles shown in Fig. 12. The chirp-parameters $\{\epsilon_p, \epsilon_q\}$ are $\{1, 0\}$ in (a, b), $\{2, 0\}$ in (c, d), and $\{0.5, 0.5\}$ in (e, f). Values of t are relative to a $|\beta'_r - \beta'_s|l$ of 10.

2. Four-wave mixing

In FWM, there are two strong pulsed pumps, each of which needs to be group-velocity-matched to a different signal channel to ensure good single-stage Green function separability. In addition, the $\chi^{(3)}$ medium being used in each stage must be long enough for complete inter-

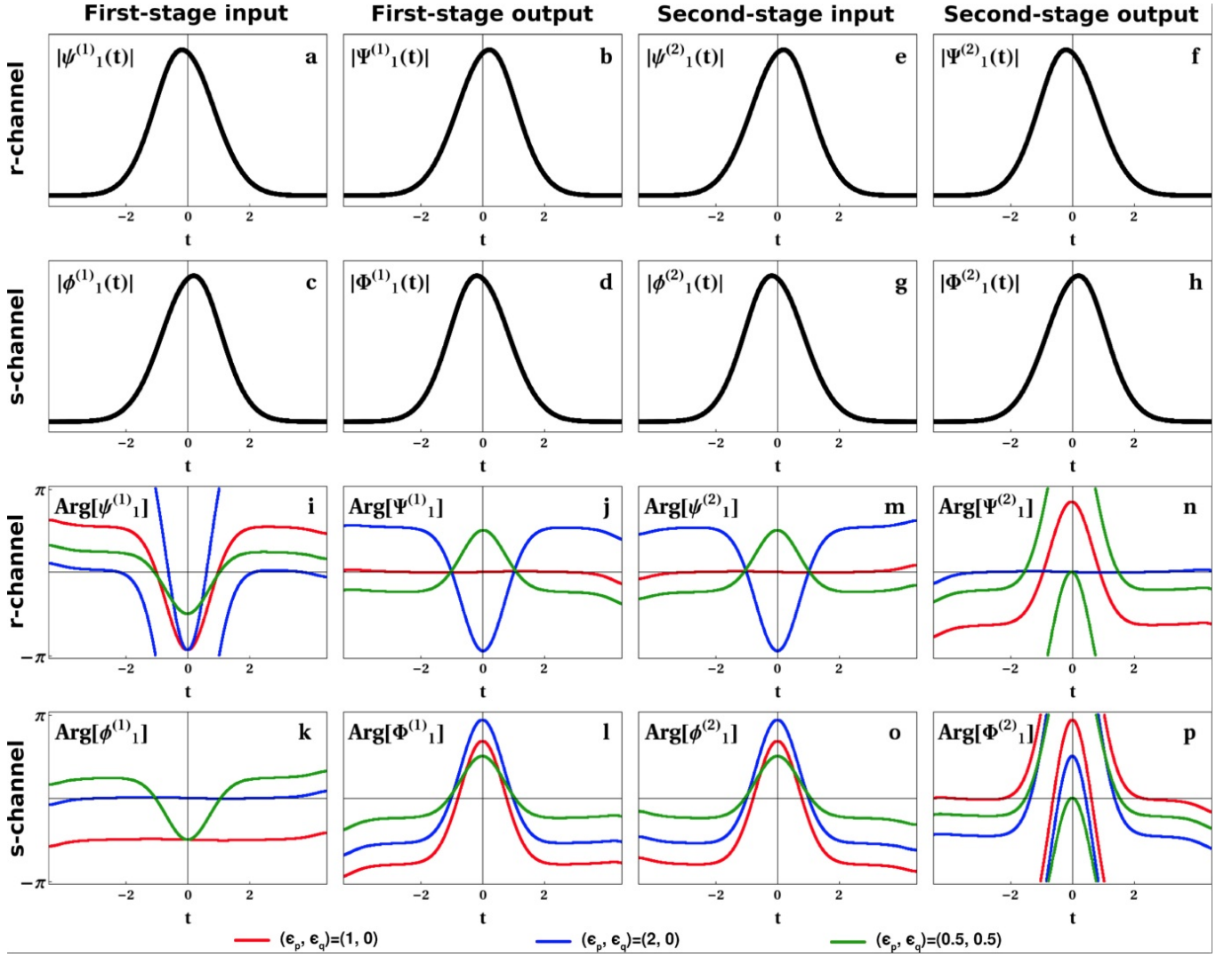


FIG. 12. The dominant input (a, c, e, g) and output (b, d, f, h) Schmidt modes for the first-(a, b, c, d) and second-(e, f, g, h) stages for both r (a, b, e, f) and s (c, d, g, h) channels for RC configuration of FWM-TMI for a Gaussian-shaped pumps, and complete pump collisions ($|\beta'_r - \beta'_s|l/(\tau_p + \tau_q) = 5$). Also shown are the corresponding Schmidt mode phase profiles (i-p) for three separate choices of pump chirps for the two stages. Due to pump-induced self- and cross-phase modulation, the second-stage pump chirps have to be related to the first-stage pump chirps in the manner specified in Eq. 16 for good inter-stage mode-matching between (b, d, j, l) and (e, g, m, o) respectively. The complete two-stage composite system Schmidt modes for FWM-TMI in the RC configuration are plotted in Fig. 13. Values of t are relative to a $|\beta'_r - \beta'_s|l$ of 10.

pump-pulse collision to occur. This is straightforward to satisfy with the use of highly-nonlinear optical fibers. For Gaussian pumps of temporal widths of the order of 10 ps, and wavelengths at 800 nm and 850 nm, a typical highly-nonlinear photonic crystal fiber will need to be about 20 m long for complete collision ($|\beta'_r - \beta'_s|l/(\tau_p + \tau_q) = 5$).

The presence of two pumps enables independent shaping of the Schmidt modes of both channels in FWM-TMI.

However, nonlinear phase modulation (Eq. 3) severely affects the Schmidt-mode phase-profiles, and restricts FWM-TMI to the RC configuration. This is a result of the well-known cross- and self-phase modulation present in any $\chi^{(3)}$ medium. To overcome this impairment, the pumps must be pre-chirped with specific phase-profiles [34] for each stage to enhance inter-stage mode-matching. The starting phase profiles of the pump p and q in stage- ξ ($\alpha_p^{(\xi)}(t)$ and $\alpha_q^{(\xi)}(t)$ respectively) need to be

$$\alpha_p^{(\xi)}(t) = -2\bar{\gamma}^{(\xi)} \int_{-\infty}^t [|\bar{A}_q(s)|^2 - |\bar{A}_p(s)|^2] ds - \frac{3}{2}\bar{\gamma}^{(\xi)} |\bar{A}_p(t)|^2 t + \frac{3}{2}\bar{\gamma}^{(\xi)} |\bar{A}_q(0)|^2 t + (\epsilon_p - \delta_{\xi,2})\gamma l |\bar{A}_p(t)|^2,$$

$$\alpha_q^{(\xi)}(t) = -2\bar{\gamma}^{(\xi)} \int_{-\infty}^t [|\bar{A}_q(s)|^2 - |\bar{A}_p(s)|^2] ds + \frac{3}{2}\bar{\gamma}^{(\xi)} |\bar{A}_q(t)|^2 t - \frac{3}{2}\bar{\gamma}^{(\xi)} |\bar{A}_p(0)|^2 t + (\epsilon_q - \delta_{\xi,2})\gamma l |\bar{A}_q(t)|^2, \quad (16)$$

where $\bar{\gamma}^{(\xi)} = \gamma/(\beta_r'^{(\xi)} - \beta_s'^{(\xi)})$, and $\bar{A}_j(t) \equiv A_j(0, t)$. The limits of the integration terms are valid only for complete pump collisions. It must be noted that the pump phase profiles contain a term each that is fully linear in time, which are equivalent to frequency shifts. These are an approximate compensation for a non-separable part of the phase profile of the GF kernels [34] which only attains significant magnitude away from the centroids of the GF-kernel amplitude functions. The slope of this term for each pump is proportional to the magnitude-square of the amplitude of the other pump's envelope. The slope is also proportional to $\bar{\gamma}^{(\xi)}$, which changes sign between the two stages. For a given set of chirp parameters, a pump will require frequency shifts of opposite signs in the two stages. Figure 11 shows the plots of the pump phase profiles from Eq. 16 for three sets of chirp parameter values. Figure 12 shows the amplitudes and phase profiles of the first input and first output Schmidt modes for both stages of FWM-TMI in the RC configuration for the same three sets of chirp parameter values.

The chirp parameters ϵ_p and ϵ_q can be any real values. However, for FWM-TMI in the RC configuration to be useful, one will have to pick specific values to make the desired channel input/output Schmidt mode have a flat phase profile. For example, Figs. 13(a)-13(d) show the Schmidt-mode amplitudes, and phases corresponding to FWM-TMI with selectivity 0.9873 ($|\rho_1|^2 = 0.9973$, $|\rho_2|^2 = 0.0082$). The pump pre-chirps (Fig. 11(c, d)) were specifically chosen to yield flat phase profiles for the r -output (Fig. 13(f)) and s -input (Fig. 13(g)) Schmidt modes. Namely, $\epsilon_p = 2$ and $\epsilon_q = 0$. The results were computed for $|\beta_r' - \beta_s'|l/(\tau_p + \tau_q) = 5$.

FWM-TMI can in principle be extended to multiple stages, provided that every stage-interface is in the RC configuration. The pump frequency shift will alternate in sign for every stage in sequence. The pump chirp profile functions in Eq. 16 will likewise need to be generalized for arbitrary number of stages. The Kronecker- $\delta_{\xi,2}$ term will pick up a factor inversely proportional to the number of stages.

The need for pump-phase chirps in FWM-TMI can be circumvented if one resorts to asymmetrically-pumped Bragg scattering [41], in which one of the pumps is made very long or continuous wave (CW), and the shorter pump power is relatively weak. Then, all self- and cross-phase modulation effects occur only due to the long CW pump, which is equivalent to pump-power-

dependent frequency and wavenumber shifts of the signals. This method can simulate TWM-like dynamics in a $\chi^{(3)}$ medium, and by extension, can be used to implement TWM-TMI using FWM. Pump-signal group-velocity matching is easier to achieve in $\chi^{(3)}$ media with waves whose interaction is phase matched, and the choice of which pump is to be made CW does not affect the selectivity, making asymmetrically pumped Bragg scattering a valuable option warranting further study.

V. V. CONCLUDING REMARKS

TMI can nearly perfectly separate field-orthogonal temporal modes into separate beams corresponding to different carrier frequencies, as well as combine such TMs into a single beam. It also enables real-time routing capabilities in all-optical networks while transcending the limitations of narrow-band filtering and projective measurement schemes [42]. It offers true field-orthogonal realizations of both classical [43] and quantum [42] optical code-division multiple-access (OCDMA) networks with high spectral efficiency for both channel routing and detection, unhindered by multiuser interference.

Breaking the 80% single-stage selectivity limit provides a means of physically realising high-fidelity quantum-unitary devices such as the proposed 'quantum pulse gate' (orthogonal-field TM sorter) and 'quantum pulse shaper' [44], which operate explicitly on the TM Hilbert-space. TMI can aid in long-distance quantum communication and quantum key distribution using novel continuous-variable encodings of qubits or qudits in the time-frequency basis [45]. The tunable interferometric phase-angle allows TMI to simulate linear optical elements analogous to the action of polarizing and non-polarizing beam splitters, half-wave plates and quarter-wave plates on the polarization basis. TMI devices can therefore perform arbitrary unitary transformations on the TM space, and in conjunction with multimode quantum memories (such as atomic Raman memories [46, 47]), open a new avenue for linear optical quantum computing in a single spatial mode [48]. All of these applications will be elaborated upon in future publications.

In conclusion, TMI can selectively manipulate photonic temporal mode components of any shape accessible by our ability to reshape strong pump pulses [49, 50]. Modular TMI devices also possess a phase control (θ)

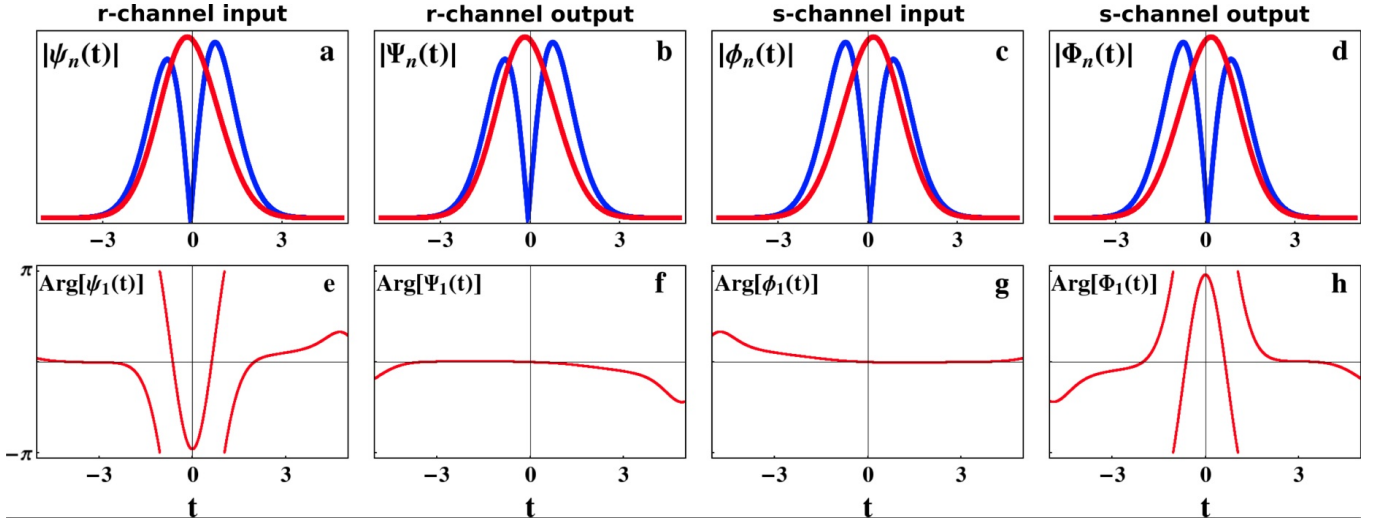


FIG. 13. The first two Schmidt modes (a, b, c, d), and first Schmidt-mode phase profiles (e, f, g, h) for FWM-TMI in the RC configuration with Gaussian pumps. The first two Schmidt modes are shown for r -input (a), r -output (b), s -input (c), and s -output (d). Pump pre-chirp parameters used were $\epsilon_p = 2$, $\epsilon_q = 0$. The selectivity was 0.9873. Values of t are relative to a $|\beta'_r - \beta'_s|l$ of 10.

that can suppress QFC completely and on demand. TMI may be implemented using either three-wave mixing, or four-wave mixing enabled frequency conversion, and may be generalized to multiple stages for gains in selectivity asymptotically approaching unity. The addition of temporal-mode analysis to polarization and orbital angular momentum analysis completes the toolkit for en-

coding information on quantum and classical states of light.

We thank L. Mejling, K. Rottwitt and J. Nunn for helpful discussions. This work was supported by the National Science Foundation through EPMD and GOALI, grant ECCS-1101811.

-
- [1] B. J. Smith and M. G. Raymer, New J. Phys. **9**, 414 (2007).
 - [2] H. Sasada and M. Okamoto, Phys. Rev. A **68**, 012323 (2003).
 - [3] T. Yarnall, A. F. Abouraddy, B. E. A. Saleh, and M. C. Teich, Phys. Rev. Lett. **99**, 250502 (2007).
 - [4] P. J. Winzer, “Modulation and multiplexing in optical communication systems,” IEEE LEOS Newsletter, **23** (1), 4 (2009).
 - [5] J. T. Barreiro, T. C. Wei, and P. G. Kwiat, Nature Phys. **4**, 282 (2008).
 - [6] G. C. G. Berkhout, M. P. J. Lavery, J. Courtial, M. W. Beijersbergen, and M. J. Padgett, Phys. Rev. Lett. **105**, 153601 (2010).
 - [7] A. M. Yao and M. J. Padgett, Adv. Opt. Photon. **3**, 161 (2011).
 - [8] J. Wang, J.-Y. Yang, I. M. Fazal, N. Ahmed, Y. Yan, H. Huang, Y. Ren, Y. Yue, S. Dolinar, M. Tur, and A. E. Willner, Nature Photon. **6**, 488 (2012).
 - [9] N. Bozinovic, Y. Yue, Y. Ren, M. Tur, P. Kristensen, H. Huang, A. E. Willner, and S. Ramachandran, Science **340**, 1545 (2013).
 - [10] Q. Yang, A. A. Amin, and W. Shieh, in *Impact of nonlinearities on Fiber Optic Communications*, edited by S. Kumar (Springer, 2011), ch. 2.
 - [11] M. Nakazawa, M. Yoshida, and T. Hirooka, Optica **1**, 15 (2014).
 - [12] U. Titulaer and R. Glauber, Phys. Rev. **145** (1966).
 - [13] H. J. McGuinness, M. G. Raymer, C. J. McKinstrie, and S. Radic, Phys. Rev. Lett. **105**, 093604 (2010).
 - [14] A. Eckstein, B. Brecht, and C. Silberhorn, Opt. Express **19**, 13770 (2011).
 - [15] I. A. Walmsley and V. Wong, J. Opt. Soc. Am. B **13**, 2453 (1996).
 - [16] D. V. Reddy, M. G. Raymer, and C. J. McKinstrie, Opt. Lett. **39**, 2924 (2014).
 - [17] C. J. McKinstrie, L. Mejling, M. G. Raymer, and K. Rottwitt, Phys. Rev. A **85**, 053829 (2012).
 - [18] L. Mejling, C. J. McKinstrie, M. G. Raymer, and K. Rottwitt, Opt. Express **20**, 8367 (2012).
 - [19] D. V. Reddy, M. G. Raymer, C. J. McKinstrie, L. Mejling, and K. Rottwitt, Opt. Express **21**, 13840 (2013).
 - [20] A. S. Kowligy, P. Manurkar, N. V. Corzo, V. G. Velez, M. Silver, R. P. Scott, S. J. B. Yoo, P. Kumar, G. S. Kanter, and Y.-P. Huang, Opt. Express **22**, 27942 (2014).
 - [21] M. G. Raymer and K. Srinivasan, Phys. Today **65**, 32 (2012).
 - [22] B. Brecht, A. Eckstein, R. Ricken, V. Quiring, H. Suche, L. Sansoni, and C. Silberhorn, Phys. Rev. A **90**, 030302 (2014).
 - [23] N. F. Ramsey, Phys. Rev. **78**, 695 (1950).

- [24] T. W. Mossberg, R. Kachru, S. R. Hartmann, and A. M. Flusberg, Phys. Rev. A **20**, 1976 (1979).
- [25] M. A. Kasevich, E. Riis, S. Chu, and R. G. DeVoe, Phys. Rev. Lett. **63**, 612 (1989).
- [26] S. Clemmen, A. Farsi, S. Ramelow, and A. L. Gaeta, in *CLEO: 2014 Postdeadline Paper Digest, paper: FTh5A.2* (Optical Society of America, 2014).
- [27] J. Huang and P. Kumar, Phys. Rev. Lett. **68**, 2153 (1992).
- [28] A. P. Vandevender and P. G. Kwiat, J. Mod. Opt. **51**, 1433 (2004).
- [29] M. A. Albota and F. N. C. Wong, Opt. Lett. **29**, 1449 (2004).
- [30] R. V. Roussev, C. Langrock, J. R. Kurz, and M. M. Fejer, Opt. Lett. **29**, 1518 (2004).
- [31] M. Rakher, L. Ma, O. Slattery, X. Tang, and K. Srinivasan, Nature Photon. **4**, 786 (2010).
- [32] A. S. Clark, S. Shahnia, M. J. Collins, C. Xiong, and B. J. Eggleton, Opt. Lett. **38**, 947 (2013).
- [33] L. E. Myers, R. C. Eckardt, M. M. Fejer, R. L. Byer, W. R. Bosenberg, and J. W. Pierce, J. Opt. Soc. Am. B **12**, 2102 (1995).
- [34] L. Mejling, D. S. Cargill, C. J. McKinstrie, K. Rottwitt, and R. O. Moore, Opt. Express **20**, 27454 (2012).
- [35] M. G. Raymer, S. J. van Enk, C. J. McKinstrie, and H. J. McGuinness, Opt. Commun. **283**, 747 (2010).
- [36] D. C. Burnham and R. Y. Chiao, Phys. Rev. **188**, 667 (1969).
- [37] O. Pfister, S. Feng, G. Jennings, R. Pooser, and D. Xie, Phys. Rev. A **70**, 020302 (2004).
- [38] C. J. McKinstrie, S. J. van Enk, M. G. Raymer, and S. Radic, Opt. Express **16**, 2720 (2008).
- [39] A. B. U'Ren, C. Silberhorn, K. Banaszek, I. A. Walmsley, R. Erdmann, W. P. Grice, and M. G. Raymer, Laser Phys. **15**, 146 (2005).
- [40] T. Søndergaard and K. H. Dridi, Phys. Rev. B **61**, 15688 (2000).
- [41] L. Mejling, S. M. M. Friis, D. V. Reddy, K. Rottwitt, M. G. Raymer, and C. J. McKinstrie, in *Advanced Photon., paper: JTu3A.36* (Optical Society of America, 2014).
- [42] A. Hayat, X. Xing, A. Feizpour, and A. M. Steinberg, Opt. Express **20**, 29174 (2012).
- [43] J. Heritage and A. Weiner, IEEE J. Sel. Top. Quantum Electron. **13**, 1351 (2007).
- [44] B. Brecht, A. Eckstein, A. Christ, H. Suche, and C. Silberhorn, New J. Phys. **13**, 065029 (2011).
- [45] J. Nunn, L. J. Wright, C. Söller, L. Zhang, I. A. Walmsley, and B. J. Smith, Opt. Express **21**, 15959 (2013).
- [46] K. Jensen, W. Wasilewski, H. Krauter, T. Fernholz, B. M. Nielsen, M. Owari, M. B. Plenio, A. Serafini, M. M. Wolf, and E. S. Polzik, Nature Phys. **7**, 13 (2011).
- [47] P. C. Humphreys, W. S. Kolthammer, J. Nunn, M. Barbieri, A. Datta, and I. A. Walmsley, Phys. Rev. Lett. **113**, 130502 (2014).
- [48] P. C. Humphreys, B. J. Metcalf, J. B. Spring, M. Moore, X.-M. Jin, M. Barbieri, W. S. Kolthammer, and I. A. Walmsley, Phys. Rev. Lett. **111**, 150501 (2013).
- [49] S. T. Cundiff and A. M. Weiner, Nature Photon. **4**, 760 (2010).
- [50] A. M. Weiner, Optics Commun. **284**, 3669 (2011).